Thin Film Flow Over and Around Surface Topography: a General Solver for the Long-Wave Approximation and Related Equations

P.H. Gaskell[1]**, Y.C. Lee**[2] **and H.M. Thompson**[1]

Abstract: The three-dimensional flow of a gravity-driven continuous thin liquid film on substrates containing micro-scale features is modelled using the long-wave lubrication approximation, encompassing cases when surface topography is either engulfed by the film or extends all the way though it. The discrete analogue of the time-dependent governing equations is solved accurately using a purpose designed multigrid strategy incorporating both automatic error-controlled adaptive time stepping and local mesh refinement/de-refinement.   Central to the overall approach is a Newton globally convergent algorithm which greatly simplifies the inclusion of further physics via the solution of additional equations of the same form as the base flow lubrication equations. The range of applicability, efficiency and flexibility of the approach is demonstrated by solving a hierarchy of problems involving variations in solute concentration and solid-fluid interactions arising from flow on flexible susbtrates.

Keywords: Thin films, occlusions, topography, long-wave approximation, multi-gridding, automatic spatial and temporal error-control.

1   Introduction

Accurately predicting the free-surface disturbance arising from three-dimensional flow of a continuous thin liquid film on substrates (man-made or naturally occurring) containing regions of mico-scale topography represents a considerable challenge, both modelling and computation wise, given that the same can persist over length scales several orders of magnitude greater than the topography itself [Decré and Baret (2003); Sellier, Lee, Thompson and Gaskell (2009)]. The problem becomes even more acute when the features concerned are (i) small, requiring very

---

[1] School of Mechanical Engineering, University of Leeds, Leeds, LS2 9JT, UK.
[2] Department of Mechanical Engineering, Heriot-Watt University, Edinburgh, EN14 4AS, UK.

fine mesh resolution, and/or (ii) heterogeneous, covering a wide surface extent, and (iii) when it is necessary to include essential additional physics.

For the sake of brevity and without appearing to seemingly dismiss the excellent body of related, though sparse, experimental work and large number of two-dimensional flow analyses that have appeared - see [Craster and Matar (2009)] and [Veremieiev, Lee, Thompson and Gaskell (2010a)] for a concise but comprehensive summary, together with the references contained therein - attention is restricted to cases of three-dimensional gravity-driven flow only and associated progress to date. It is not surprising, given the complexity involved, the two principal methods of addressing such problems computationally to emerge involve either a long-wave approximation of the governing Navier-Stokes equations or the assumption at the outset of steady-state Stokes flow. With regard to the latter the first and important contribution, and one which remained so for several years, is the that of [Pozrikidis and Thoroddsen (1991)]. They showed, using a boundary integral equation formulation of the governing equations, that flow over a particle-like topography resulted, as observed experimentally by [Peurrung and Graves (1991)] when spin coating, in a significant upstream and downstream free-surface disturbance comprised of a 'bow wave' capillary ridge and an exponentially decaying 'horseshoe'-shaped capillary wake.

The above boundary integral equation approach has since been refined further and an error in its earlier formulation corrected by [Blyth and Pozrikidis (2006)], who used it to investigate the related problem of flow over a fully submerged three-dimensional obstacle. More recently [Baxter, Power, Cliffe and Hibberd (2009)], motivated by thin films in the context of surface cooling and the work of [Sellier, Lee, Thompson and Gaskell (2009)] addressing film flow when topography in the form of occlusions is present, see below, have taken the boundary integral formulation a stage further. The key features of the approach of the former is the use of a Hermitian radial basis function to evaluate the free-surface terms and elimination of the restriction of small free-surface deformation, thus enabling accurate results to be obtained in the case of large obstacles lying either within or protruding through a liquid film.

Turning now to work based on the long-wave, or lubrication, approximation, arguably the first comprehensive and detailed computational study of three-dimensional thin film flow over surface topography was performed by [Gaskell, Jimack, Sellier, Thompson and Wilson (2004)]. The results they obtained, using a very efficient purpose designed multigrid algorithm embodying automatic error-controlled time stepping [Gaskell, Jimack, Sellier and Thompson (2004)] to solve an implicit finite-difference analogue for the film thickness and pressure, were found to be in excellent agreement with the corresponding experiments of [Decré and Baret (2003)],

to within the experimental error reported, and to similarly capture all of the associated free-surface features mentioned above. They also quantified the expected error from the neglect of inertia, and the effect of substrate inclination angle and topography aspect ratio. In addition, they were able to establish the appropriateness of the theory underpinning the earlier linear analysis of [Hayes, O'Brien and Lammers (2000)]; namely, that when inertia is negligibly small, superposition can be used to construct an appropriate free-surface response to complex topography from the knowledge of the responses to regular elementary topographies.

This multigrid methodology has since been developed and refined considerably to incorporate automatic errror controlled local mesh adoption and to include additional physical effects such as evaporation [Gaskell, Jimack, Sellier and Thompson (2006)] and substrate flexibility [Lee, Thompson and Gaskell (2009)]. It has also been used to investigate the effect of complex topography in relation to the severity of the resulting free-surface disturbance, as well as the impact of occlusions within the flow domain [Lee, Thompson and Gaskell (2008)]. The latter feature was investigated subsequently in more detail, [Sellier, Lee, Thompson and Gaskell (2009)], for a variety of occlusion configurations and comparisons drawn with equivalent complementary finite element solutions of the weak form of the lubrication equations obtained using a commercially available software package [COMSOL (2008)].

The present paper describes a numerical procedure which simplifies the inclusion of further physics into lubrication analyses of three-dimensional gravity driven thin film flow over surface topography. The strategy adopted provides a holistic approach for the posing and accurate solution of these and similar flow problems and represents a general purpose and efficient numerical solver for degenerate equations of the lubrication type. The problems of interest and associated mathematical models are outlined in section 2. This is followed by a description of the overall numerical algorithm formulated to generate solutions both flexibly and efficiently in section 3. A comprehensive set of results is presented in section 4 with conclusions drawn in section 5.

2 Problem Specification

2.1 Mathematical Model

Consider for illustrative purposes, as shown in Fig. 1, the simple case of a time-dependent gravity driven film flow, of constant flux Q_0 per unit width and asymptotic thickness H_0, down a planar surface containing a well-defined topography/occlusion, of depth/height S_0, length $L_T (\ll L_S)$ and width $W_T (\gg W_S)$, that is inclined at an angle $\theta (\neq 0)$ to the horizontal. The film will either flow over ($S_0 < H_0$) or around
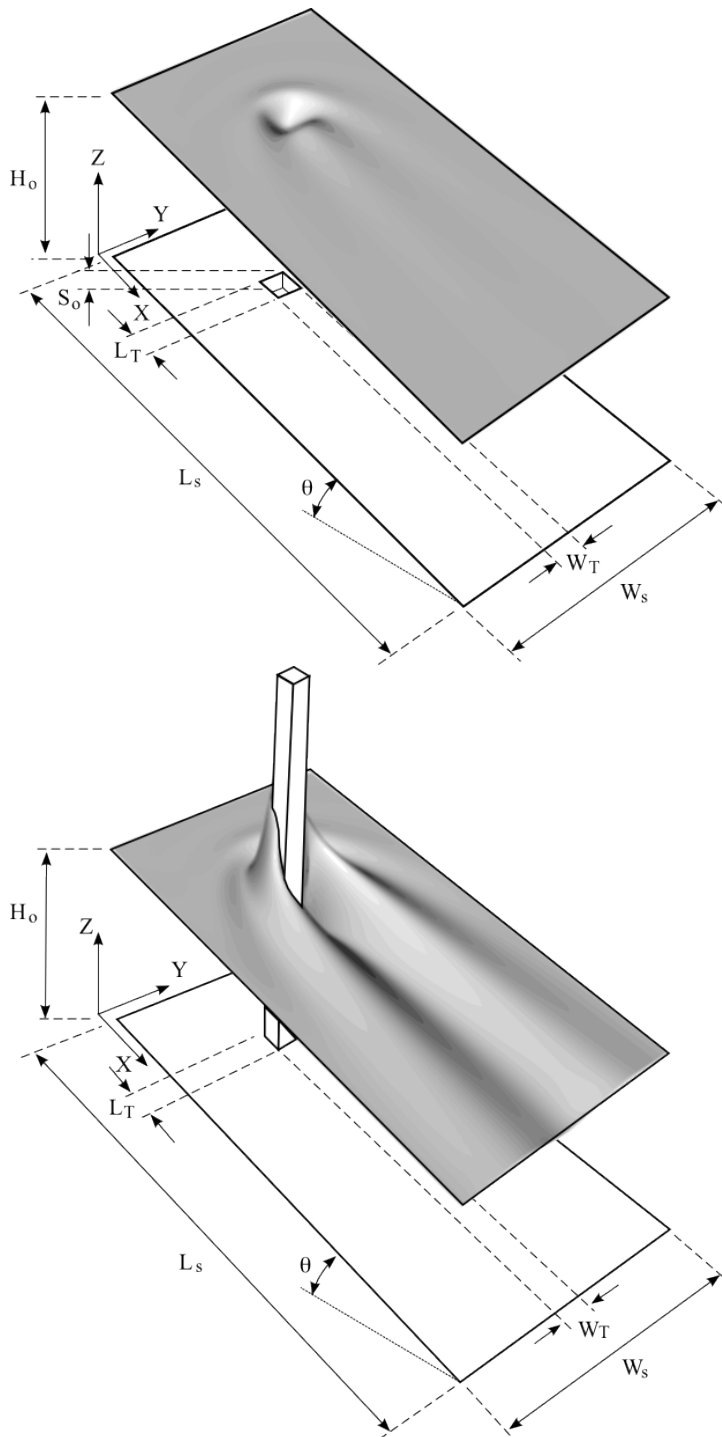
Figure 1: Gravity-driven thin film flow: (a) over a small square trench ($S_0 < H_0$) and (b) past a square occlusion ($S_0 \geq H_0$). Schematic of the flow domain and defining geometry.

($S_0 \gg H_0$) the feature. The liquid is assumed Newtonian and incompressible, with constant viscosity, μ, density, ρ, and surface tension, σ. The chosen Cartesian steamwise, X, spanwise, Y, and normal, Z, coordinates are as indicated and the solution domain is bounded from below by the inclined surface $S(X,Y)$ and from above at time T by the free-surface $F(X,Y,T)$. The film thickness, $H(X,Y,T)$, at any point in the (X,Y) plane is given by $H = F - S$ and the resulting laminar flow is described by the Navier-Stokes and continuity equations, namely:

$$\rho \left(\frac{\partial U}{\partial T} + \underline{U}.\nabla \underline{U} \right) = -\nabla P + \mu \nabla^2 \underline{U} + \rho \underline{g} , \tag{1}$$

$$\nabla.\underline{U} = 0 , \tag{2}$$

where $\underline{U} = (U,V,W)$ and $P(X,Y,T)$ are the fluid velocity and pressure, respectively and $\underline{g} = g(\sin\theta, 0, -\cos\theta)$ is the acceleration due to gravity where g is the standard gravity constant.

The task of solving the above equations together with appropriate boundary conditions, written in non-dimensional form using the following scalings:

$$h = \frac{H}{H_0}, \quad f = \frac{F}{H_0}, \quad s = \frac{S}{H_0}, \quad (x,y,z) = (\frac{X}{L_0}, \frac{Y}{L_0}, \frac{Z}{H_0}),$$

$$p = \frac{2P}{\rho g L_0 \sin\theta}, \quad (u,v,w) = (\frac{U}{U_0}, \frac{V}{U_0}, \frac{W}{\varepsilon U_0}), \quad t = \frac{U_0 T}{L_0},$$

is simplified considerably by employing the long-wave approximation, effectively reducing the dimensionality of the problem by one. The lower-case variables have the same meaning as their dimensional counterparts; while U_0 ($= \frac{3Q_0}{2H_0}$, with $Q_0 = \frac{H_0^3 \rho g \sin\theta}{3\mu}$), the surface velocity of the undisturbed fully developed film, and L_0 (with $\varepsilon = \frac{H_0}{L_0} \ll 1$) are the characteristic velocity and in-plane length scales, respectively. The latter, following previous work [Decré and Baret (2003)], is expressed in terms of the capillary length-scale, L_c, as:

$$L_0 = \beta L_c = \beta \left(\frac{\sigma H_0}{3\rho g \sin\theta} \right)^{1/3} , \tag{3}$$

where β is a constant of proportionality. The required lubrication equation for the film thickness, h, is obtained by first expanding equations (1) and (2) in terms of ε, neglecting terms of $O(\varepsilon^2)$ and smaller, and imposing no-slip and zero tangential stress conditions at $z = s$, and $z = f$, respectively; next, integrating the resulting expressions for u and v between these limits gives the flux vector $\underline{q} = (q_x, q_y)^T$,

where:

$$q_x = -\frac{h^3}{3\mu}\left(\frac{\partial p}{\partial x} - 2\right), \quad q_y = -\frac{h^3}{3\mu}\left(\frac{\partial p}{\partial y}\right) , \tag{4}$$

with the pressure, taking the pressure datum to be zero, given by:

$$p = -\frac{6}{\beta^3}\nabla^2(f) + \frac{2}{\beta}6^{1/3}N(f-z) ; \tag{5}$$

$N = Ca^{1/3}\cot\theta$, for fixed liquid properties indicating the influence of the normal component of gravity, while $Ca = \frac{\mu U_0}{\sigma}$ $(= \frac{\varepsilon^3}{6} = \frac{H_0^3}{6L_0^3} \ll 1)$ is the Capillary number. Accordingly, the lubrication equation takes the form

$$\frac{\partial f}{\partial t} = -\nabla \cdot \underline{q} = \frac{\partial}{\partial x}\left[\frac{h^3}{3}\left(\frac{\partial p}{\partial x} - 2\right)\right] + \frac{\partial}{\partial y}\left[\frac{h^3}{3}\left(\frac{\partial p}{\partial y}\right)\right] . \tag{6}$$

Equations (5) and (6) can be combined to yield a single fourth order equation [Diez and Kondic (2002)]; however, solving them separately is preferred since experience suggests, and as reported elsewhere [Trottenberg, Oosterlee and Schüller (2001)], that within the chosen multigrid framework described later, this enables much larger time-steps to be taken [Daniels, Ehret, Gaskell, Thompson and Decré (2001)]. Note that, as shown quantitatively in [Gaskell, Jimack, Sellier, Thompson and Wilson (2004)] and subsequently by [Veremieiev, Lee, Thompson and Gaskell (2010a)], lubrication theory leads to an accurate description of the flows of interest for small Reynolds number and provided, in the case of submerged topography, that s_0 is not too large.

The boundary conditions required to close the problem are that the flow is fully developed both upstream and downstream:

$$f(x=0,y) = 1 , \frac{\partial f}{\partial x}|_{x=0} = 0, \frac{\partial f}{\partial x}|_{x=1} = \frac{\partial p}{\partial x}|_{x=1} = 0, \tag{7}$$

together with the requirement of zero flux at the boundaries in the spanwise direction:

$$\frac{\partial p}{\partial y}|_{y=0} = \frac{\partial p}{\partial y}|_{y=1} = \frac{\partial f}{\partial y}|_{y=0} = \frac{\partial f}{\partial y}|_{y=1} = 0. \tag{8}$$

When occlusions are present within the flow the following boundary condition is applied at the associated static wetting line [Lee, Thompson and Gaskell (2008)]:

$$\nabla f_w \cdot \underline{n} = \frac{1}{\varepsilon}\tan\left(\theta_s - \frac{\pi}{2}\right) , \tag{9}$$

where $f_w(x, y)$ denotes the static wetting line formed at the occlusion, $\underline{n}$ is the outward pointing unit normal at the surface of the occlusion and θ_s the static contact angle, which in the present work is prescribed to be 90°. The effect of varying static contact angle has been considered by [Baxter, Power, Cliffe and Hibberd (2009)]. The remaining constraint at the occlusion surface is modelled within the lubrication framework by a no-flux condition, which is imposed by specifying that the flux, q_s, given by equation (4) is zero there, i.e.

$$\underline{q}_s = -\frac{h^3}{3}(\nabla p - 2\mathbf{i}) = 0 \,. \tag{10}$$

The recent investigation of [Veremieiev, Thompson, Lee and Gaskell (2010b)], using a depth averaged form of the Navier-Stokes equations to explore film flow on planar substrates containing occlusions, has shown this no-flux condition to be equivalent to applying the common and more strictly rigorous no-slip boundary condition along the surface of an occlusion.

Topography is defined via arctangent functions [Stillwagon and Larson (1988)] enabling the creation of simple primitive shapes. For example, a rectangular trench/peak topography of length l_t, width w_t and depth/height $|s_0|$ centred at (x_t, y_t) has the form:

$$s(x, y) = \frac{s_0}{b_0} \left[\tan^{-1}\left(\frac{-a_x - l_t/2}{\gamma l_t}\right) + \tan^{-1}\left(\frac{a_x - l_t/2}{\gamma l_t}\right)\right] \times \\ \left[\tan^{-1}\left(\frac{-a_y - w_t/2}{\gamma w_t}\right) + \tan^{-1}\left(\frac{a_y - w_t/2}{\gamma w_t}\right)\right], \tag{11}$$

where γ is an adjustable parameter whose value specifies the steepness of the topography, while $a_x = x_t - x$, and $a_y = y_t - y$ are the latter's local coordinates in the x and y directions, respectively; $A = w_t/l_t$ is the aspect ratio of the topography with:

$$b_0 = 4\tan^{-1}\left(\frac{1}{2\gamma}\right)\tan^{-1}\left(\frac{A}{2\gamma}\right) \,. \tag{12}$$

Equation (11) can, as in the present work, be used to create a variety of simple primitive topographies by modifying a_x and a_y accordingly. It is relatively straight forward to create more complex topographical features by combining such simple primitive shapes [Lee, Thompson and Gaskell (2007)].

2.2 Incorporating additional physics

In many thin film flows of practical interest physical effects such as solute transport, evaporation, thermal gradients, substrate flexibility, etc., are significant. The

equations describing these features may be stand alone, form a coupled set and/or be linked to the flow equations themselves.

Considering all possible physical effects is clearly beyond the scope of the present work. Instead the focus is the design of an efficient methodology enabling the seamless incorporation of any number of such equations and their effective solution within the multigrid framework described subsequently. The applicability of the overall approach is demonstrated via the solution of a hierarchy of problems incorporating one or both of the following additional physical effects: (i) solute transport; (ii) substrate flexibility. The extra equations involved are given below.

2.2.1   Solute Transport

The well-mixed approximation [Howison, Moriarty, Ockendon, Terril and Wilson (1997)] that the diffusion of solute is sufficiently rapid so that its concentration, c, can be assumed to be uniform across the film, fits naturally within the lubrication framework. For a liquid whose viscosity can be assumed to be independent of solute concentration, the governing advection diffusion equation [Gaskell, Jimack, Sellier and Thompson (2006)] is:

$$\frac{\partial c}{\partial t} = \left[\frac{h^2}{3\mu}\left(\frac{\partial p}{\partial x} - 2\right)\right]\frac{\partial c}{\partial x} + \left[\frac{h^2}{3\mu}\left(\frac{\partial p}{\partial y}\right)\right]\frac{\partial c}{\partial y} + \frac{d}{h}\nabla \cdot (h\nabla c) , \tag{13}$$

with $d = D/L_0 U_0$ denoting the dimensionless solvent diffusivity. If in addition, the lateral diffusion is dominated by convection, that is $D \ll LU_0$, equation (13) simplifies further:

$$\frac{\partial c}{\partial t} = \left[\frac{h^2}{3\mu}\left(\frac{\partial p}{\partial x} - 2\right)\right]\frac{\partial c}{\partial x} + \left[\frac{h^2}{3\mu}\left(\frac{\partial p}{\partial y}\right)\right]\frac{\partial c}{\partial y} . \tag{14}$$

2.2.2   Substrate Flexibility

Substrate flexibility can be accounted for by relating its deflection, $e = E/H_0$, and $f = h + s + e$, to the corresponding hydrostatic and capillary pressures exerted by the liquid film via a direct application of Newton's second law [Lee, Thompson and Gaskell (2009)]. With the flexible substrate taken to be homogeneous, infinitely long and thin (thickness λ) with uniform tension, ζ, in the longitudinal and transverse directions, to have constant density, ρ_m, and damping coefficient, η, then within the limits of the lubrication approximation ($\varepsilon \ll 1$) the equation to be solved is:

$$-\Upsilon\left(\frac{\partial^2 e}{\partial x^2} + \frac{\partial^2 e}{\partial y^2}\right) = -\left(f + \frac{\rho_m}{\rho}\lambda\right)\text{Bo}\cos\theta + \frac{\partial^2 f}{\partial x^2} + \frac{\partial^2 f}{\partial y^2} , \tag{15}$$

where $\mathrm{Bo} = \rho g L_0^2 / \sigma$ is the Bond number measuring the ratio of gravitational to surface tension forces, and $\Upsilon = \zeta / \sigma$ is the ratio of tension in the flexible substrate to the surface tension of the liquid. Equation (15), unlike equations (6) and (14), contains no time derivative terms – this is by virtue of the scaling adopted which results in such terms having the pre-factor ε^2.

The additional boundary conditions required to close the problem following incorporation of either, or both, of the above physical effects are:

$$c(x = 0, y) = c_0 \quad \text{and} \quad e(x = 0, y) = 0, \tag{16}$$

for concentration and substrate deflection, respectively.

3   Method of Solution

In what follows only the new key features of the proposed general overall numerical procedure are provided in detail, with just an overview given of the other salient points since they are described in considerable detail elsewhere.

3.1   Spatial Discretisation

Equations (5) and (6), together with equations (14) and (15), written in the form of the following finite-difference analogues, are solved at each node (i, j) of a rectangular computational domain, $(x, y) \in \Omega$, with equal, uniform grid spacings, Δ, in the x and y directions:

$$
\begin{aligned}
\frac{\partial f_{i,j}}{\partial t} = {} & \frac{1}{\Delta^2} \left[\frac{h^3}{3} \bigg|_{i+\frac{1}{2},j} (p_{i+1,j} - p_{i,j}) - \frac{h^3}{3} \bigg|_{i-\frac{1}{2},j} (p_{i,j} - p_{i-1,j}) + \right. \\
& \left. \frac{h^3}{3} \bigg|_{i,j+\frac{1}{2}} (p_{i,j+1} - p_{i,j}) - \frac{h^3}{3} \bigg|_{i,j-\frac{1}{2}} (p_{i,j} - p_{i,j-1}) \right] - \\
& \frac{2}{\Delta} \left(\frac{h^3}{3} \bigg|_{i+\frac{1}{2},j} - \frac{h^3}{3} \bigg|_{i-\frac{1}{2},j} \right),
\end{aligned}
\tag{17}
$$

$$p_{i,j} = -\frac{6}{\beta^3 \Delta^2} \left[f_{i+1,j} + f_{i-1,j} + f_{i,j+1} + f_{i,j-1} - 4f_{i,j} \right] + \frac{2\sqrt[3]{6}N}{\beta} f_{i,j}, \tag{18}$$

$$
\begin{aligned}
\frac{\partial c_{i,j}}{\partial t} = {} & \frac{h_{i,j}^2}{12\Delta^2} \left[(p_{i+1,j} - p_{i-1,j})(c_{i+1,j} - c_{i-1,j}) + \right. \\
& \left. (p_{i,j+1} - p_{i,j-1})(c_{i,j+1} - c_{i,j-1}) \right] - \frac{h_{i,j}^2}{3\Delta}(c_{i+1,j} - c_{i-1,j}),
\end{aligned}
\tag{19}
$$

$$
e_{i,j} = \frac{1}{4}\left(e_{i+1,j}+e_{i-1,j}+e_{i,j+1}+e_{i,j-1}\right) - \frac{\Delta^2}{4\Upsilon}\left[\left(f_{i,j}+\frac{\rho_m}{\rho_f}\lambda_{i,j}\right)\text{Bo}\cos\theta + \right.
$$
$$
\left.\left(\frac{f_{i+1,j}+f_{i-1,j}+f_{i,j+1}+f_{i,j-1}-4f_{i,j}}{\Delta^2}\right)\right].
\tag{20}
$$

The $\frac{h^3}{3}\big|_{i\pm\frac{1}{2},j}$ and $\frac{h^3}{3}\big|_{i,j\pm\frac{1}{2}}$ terms are obtained from linear interpolation between neighbouring nodes.

Time integration is performed using the second-order accurate Crank-Nicholson method to approximate the time-derivative in equations (17) and (19). Re-writing the right-hand-sides of equations (6) and (14) as functions, $\mathscr{R}^f$ and $\mathscr{R}^c$, respectively of the dependent variables involved, leads to equations of the form:

$$
f_{i,j}^{n+1} - \frac{\Delta t^{n+1}}{2}\mathscr{R}^f\left(h_{i,j}^{n+1},p_{i,j}^{n+1},h_{i\pm1,j}^{n+1},p_{i\pm1,j}^{n+1},h_{i,j\pm1}^{n+1},p_{i,j\pm1}^{n+1}\right)
$$
$$
= f_{i,j}^n + \frac{\Delta t^{n+1}}{2}\mathscr{R}^f\left(h_{i,j}^n,p_{i,j}^n,h_{i\pm1,j}^n,p_{i\pm1,j}^n,h_{i,j\pm1}^n,p_{i,j\pm1}^n\right),
\tag{21}
$$

$$
c_{i,j}^{n+1} - \frac{\Delta t^{n+1}}{2}\mathscr{R}^c\left(h_{i,j}^{n+1},p_{i,j}^{n+1},c_{i,j}^{n+1},h_{i\pm1,j}^{n+1},p_{i\pm1,j}^{n+1},c_{i\pm1,j}^{n+1},h_{i,j\pm1}^{n+1},p_{i,j\pm1}^{n+1},c_{i,j\pm1}^{n+1}\right)
$$
$$
= c_{i,j}^n + \frac{\Delta t^{n+1}}{2}\mathscr{R}^c\left(h_{i,j}^n,p_{i,j}^n,c_{i,j}^n,h_{i\pm1,j}^n,p_{i\pm1,j}^n,c_{i\pm1,j}^n,h_{i,j\pm1}^n,p_{i,j\pm1}^n,c_{i,j\pm1}^n\right),
\tag{22}
$$

where $\Delta t^{n+1} = t^{n+1} - t^n$ and the right hand sides of the above equations are expressed in terms of known variables at the end of the *n*th time step, $t = t^n$.

3.2 Multigrid Strategy

Following the multigrid approach employed in [Lee, Thompson and Gaskell (2007)], a sequence of progressively finer grids ($\mathscr{G}_k$: $k = 0,1,...,K$), with uniform grid spacing Δ_k, is defined. Each grid level, $\mathscr{G}_k$, has $n_k = 2^{k+k_c+1} + 1$ nodes per unit length in both co-ordinate directions where k_c is a constant defining the resolution of the coarsest grid level, such that the mesh size associated with it and that on finer grid levels is $\Delta_k = 2^{-(k+k_c+1)}$. For example, the underlying coarse global grid when $k = 0$, using a coarse grid parameter $k_c = 4$, corresponds to uniform grid spacing $\Delta_0 = 1/32$. The associated time-dependent, nonlinear, coupled set of governing lubrication equations together with any extra equations embodying additional physics are solved efficiently using a combined full approximation storage (FAS) and Full Multigrid (FMG) technique.

Relaxation/smoothing on grid $\mathscr{G}_k$ is performed using a fixed number of pre- and post- Red-Black Gauss-Seidel Newton iterations. With **u** representing the vector

of unknowns of the equation set (18) plus (20) to (22) the same can be expressed more generally as:

$$\mathscr{N}_k(\mathbf{u}_k^{n+1}) = \mathscr{F}_k(\mathbf{u}_k^n) \tag{23}$$

where $\mathscr{N}_k = (\mathscr{N}_k^f, \mathscr{N}_k^p, \mathscr{N}_k^c, \mathscr{N}_k^e)$, $\mathbf{u_k} = (f_k, p_k, c_k, e_k)^T$, $\mathscr{F}_k = (r_k^f, r_k^p, r_k^c, r_k^e)$ and r_k corresponding to the right-hand-side of the above equations; the solution in the form of a linearised Newton iterative step on $\mathscr{G}_k$ can then be written as:

$$\Delta\mathbf{u_k} = \mathscr{J}_k^{-1}(\mathscr{F}_k(\mathbf{u}_k^n) - \mathscr{N}_k(\mathbf{u}_k^{n+1})) \ , \tag{24}$$

where $\mathscr{J}_k$ is the Jacobian of the system. The latter is solved simultaneously for the increments $\Delta\mathbf{u}_k$, which in turn are used to obtain a new approximation for the discretised solution on $\mathscr{G}_k$, as:

$$\tilde{\mathbf{u}}_k^{n+1} = \mathbf{u}_k^{n+1} + \Delta\mathbf{u}_k \ , \tag{25}$$

a process that is repeated at all points of the solution domain on $\mathscr{G}_k$.

The relaxation/smoothing process requires the determination of $\mathscr{J}_k$ together with its inverse. For the solution of equations (5) and (6) only, this was done in the past by expressing the component derivative terms forming the elements of $\mathscr{J}_k$ analytically. The same procedure was followed when investigating the effects of evaporation on gravity-driven film flows over topography [Gaskell, Jimack, Sellier and Thompson (2006)], which required the solution of an additional transport equation coupled to the flow equations via a solute concentration dependent viscosity.

The disadvantages and hence loss of generality inherent in the above approach is that: (i) every time an existing equation within an equation set is modified or one or more other equations representing a different physical effect are added to it, the associated Newton iterative step has to be re-written/written manually and hard-coded into the overall solver; (ii) as the number of simultaneous linear equations to be solved for numerically and the level of interdependence between them increases the provision of a good initial guess from which to begin iterating becomes restrictively more important; (iii) for a given equation set, it may not always be possible to derive analytic expressions for all of the elements forming $\mathscr{J}_k$.

Clearly, a more robust and flexible approach is required in order to arrive at a more generally applicable numerical procedure, one which is capable of solving any number of such equations, coupled or otherwise, easily, removing the need for modifications to the underlying algorithm. In the present work this goal is achieved by solving the equations using the Newton method, while at the same time avoiding the solution descending into a local minimum, as described below.

3.3   A General Newton Globally Convergent Solver

A problem having N_i transport equations, involving $u_{i,k}$ unknowns for $i = 1, 2, 3, ...N_i$ on $\mathscr{G}_k$, can be written as:

$$g_{i,k}(u_1, u_2, ..., u_{N_i}) = 0 , \tag{26}$$

where $g_{i,k}$ denotes the number of equations or functions that need to be solved simultaneously. In the present context, c.f. equation (23), these can be written as:

$$\mathbf{g}_k(\mathbf{u}_k) = \mathscr{N}_k(\mathbf{u}_k^{n+1}) - \mathscr{F}_k(\mathbf{u}_k^n) = 0, \tag{27}$$

in which $\mathbf{u}_k$ denote the vector of $u_{i,k}$ unknowns and $\mathbf{g}_k$ represents the system of residual equations to be minimised.

With regard to equations (5), (6), (14) and (15), the corresponding residual equation (27) in each case will be:

$$
\begin{aligned}
g_{1,k} &= \mathscr{N}_k^p(\mathbf{u}_k^{n+1}) - \mathscr{F}_k^p(\mathbf{u}_k^n) = 0, \\
g_{2,k} &= \mathscr{N}_k^f(\mathbf{u}_k^{n+1}) - \mathscr{F}_k^f(\mathbf{u}_k^n) = 0, \\
g_{3,k} &= \mathscr{N}_k^c(\mathbf{u}_k^{n+1}) - \mathscr{F}_k^c(\mathbf{u}_k^n) = 0, \\
g_{4,k} &= \mathscr{N}_k^e(\mathbf{u}_k^{n+1}) - \mathscr{F}_k^e(\mathbf{u}_k^n) = 0.
\end{aligned}
$$

Employing a Newton approach, based on forward-differences, and neglecting terms of order $(\Delta \mathbf{u}_k)^2$ and higher, leads to:

$$\mathbf{g}_k(\mathbf{u}_k + \Delta \mathbf{u}_k) = \mathbf{g}_k(\mathbf{u}_k) + \mathscr{J}_k \cdot \Delta \mathbf{u}_k , \tag{28}$$

where $\mathbf{g}_k(\mathbf{u}_k + \Delta \mathbf{u}_k) = 0$, so that one obtains a system of linear equations for the Newton step, c.f. equation (24), of the form:

$$\Delta \mathbf{u}_k = - \mathscr{J}_k^{-1} \cdot \mathbf{g}_k(\mathbf{u}_k) , \tag{29}$$

which is solved by LU decomposition. The corrections are then added to the solution vector as per equation (25).

Each derivative in the Jacobian, $\mathscr{J}_k$, is computed numerically from the forward difference approximation, equation (28), in which a small value $\chi \sim 10^{-8}$ is added individually to each variable in $\mathbf{u}_k$ to yield:

$$\mathscr{J}_k \approx \frac{\mathbf{g}_k(\mathbf{u}_k + \chi) - \mathbf{g}_k(\mathbf{u}_k)}{\chi} . \tag{30}$$

The solution $\Delta \mathbf{u}_k$ of equation (29) above relies on the assumption that it is relatively smooth, so as to provide a good initial guess for $\mathbf{g}_k(\mathbf{u}_k)$. In such a situation a reasonable strategy to ensure convergence is to require that the Newton step decreases the product:

$$\xi_k = \frac{1}{2} \mathscr{J}_k^2 \cdot (\Delta \mathbf{u}_k)^2 = \frac{1}{2} \mathbf{g}_k(\mathbf{u}_k) \cdot \mathbf{g}_k(\mathbf{u}_k) \ , \tag{31}$$

which at the same time provides a descent direction for ξ_k, such that its gradient satisfies:

$$\nabla \xi_k \cdot \Delta \mathbf{u}_k = (\mathbf{g}_k(\mathbf{u}_k) \cdot \mathscr{J}_k) \cdot (-\mathscr{J}_k^{-1} \cdot \mathbf{g}_k(\mathbf{u}_k)) = -\mathbf{g}_k(\mathbf{u}_k) \cdot \mathbf{g}_k(\mathbf{u}_k) < 0 \ . \tag{32}$$

Therefore, when close to the required solution, the system of equations is solved using a full Newton step, which converges quadratically and ensures that ξ_k decrease.

If at any stage, the conditions in equations (31) and (32) are violated, a backtracking routine is performed along the Newton direction to minimise ξ_k until an acceptable Newton step can be identified from which the roots of $\mathbf{g}_k(\mathbf{u}_k)$ can be found. The backtracking algorithm is employed to determine an appropriate size of $\Delta \mathbf{u}_k$ required to reduce ξ_k at each iteration and follows the suggestion of [Press, Teukolsky, Vetterling and Flannery (2003)]. A search is performed along the Newton direction such that:

$$\mathbf{u}_{k,new} = \mathbf{u}_{k,old} + \eta \Delta \mathbf{u}_k \ ; \qquad 0 < \eta \leq 1 \ , \tag{33}$$

in order to find an appropriate value of η so that $\xi_k(\mathbf{u}_{k,new})$ decreases sufficiently. By defining

$$\psi_k(\eta) \equiv \xi_k(\mathbf{u}_{k,old} + \eta \Delta \mathbf{u}_k) \ , \tag{34}$$

so that

$$\psi_k'(\eta) = \nabla \xi_k \cdot \Delta \mathbf{u}_k \ , \tag{35}$$

the backtracking strategy is initialised by making use of the current solution, with ($\eta = 1$) and without ($\eta = 0$) a full Newton step, to determine new values for η that minimise equation (35).

The first backtracking step is performed using a quadratic representation of ψ_k in terms of η:

$$\psi_k(\eta) \approx \left[\psi_k(1) - \psi_k(0) - \psi_k'(0) \right] \eta^2 + \psi_k(0)\eta + \psi_k(0) \ , \tag{36}$$

whose value is a minimum when:

$$\eta = -\frac{\psi_k(0)}{2\left[\psi_k(1) - \psi_k(0) - \psi'_k(0)\right]} \; . \tag{37}$$

In subsequent backtracking operations, a cubic representation is employed, utilising the previous value $\psi_k(\eta_1)$ and its predecessor $\psi_k(\eta_2)$:

$$\psi_k(\eta) \approx c_1\eta^3 + c_2\eta^2 + \psi_k(0)\eta + \psi_k(0) \; , \tag{38}$$

where:

$$\begin{bmatrix} c_1 \\ c_2 \end{bmatrix} = \frac{1}{\eta_1 - \eta_2} \begin{bmatrix} 1/\eta_1^2 & -1/\eta_2^2 \\ -\eta_2/\eta_1^2 & \eta_1/\eta_2^2 \end{bmatrix} \cdot \begin{bmatrix} \psi_k(\eta_1) - \psi'_k(0)\eta_1 - \psi_k(0) \\ \psi_k(\eta_2) - \psi'_k(0)\eta_2 - \psi_k(0) \end{bmatrix} \; . \tag{39}$$

The minimum of the cubic expression, equation (38), is given by:

$$\eta = \frac{-c_2 + \sqrt{c_2^2 - 3c_1\psi'_k(0)}}{3c_1} \; . \tag{40}$$

in which $0.1\eta_1 \leq \eta \leq 0.5\eta_1$.

3.4   *Spatial and Temporal Adaptivity*

Another key component of the solution strategy is the inclusion of both error controlled spatial and temporal adaptivity, the former automatically determines where fine grids are needed to capture details of a rapidly evolving flow. Adaptive grid refinement is implemented via a relative local truncation error $\tau_k^{k-1} \geq \varepsilon$, where ε is a user-specified tolerance; large values of τ_k^{k-1} indicating regions of significant error between solutions on successive grid levels and where corresponding further local mesh refinement is required. For further details the reader is referred to [Lee, Thompson and Gaskell (2007)].

Automatic adaptive time-stepping, on the other hand, is achieved by employing a temporal error control algorithm based on predictor-corrector stages, as explained in [Gaskell, Jimack, Sellier and Thompson (2004)]. The method employed provides an implicit and second order accurate alternative to existing schemes, see for example [Diez and Kondic (2002)], by using time-stepping based on local error estimates, obtained from the difference between the current and predicted solutions and which act as an indicator of whether to increase or decrease the time step in a controlled manner. This provides an efficient means of minimising the computational expense associated with repeated time step failure.

4   Results and Discussion

Solutions to a sequence of gravity-driven thin film flow problems, ranging in com-
plexity from the simple case of flow past a single well defined occlusion to ones
involving multiple occlusions/complex topography, solute transport and/or sub-
strate flexibility, are presented and explored. In all cases the substrate is taken
to be inclined at 30° to the horizontal and the initial condition before integrat-
ing forward in time to a final steady-state is that of a planar free-surface, namely
$f = 1$, everywhere. The liquid involved in the majority of cases is water (viscosity,
$\mu = 0.001$ Pa s, density, $\rho = 1000$ kg m^{-3} and surface tension, $\sigma = 0.07$ N m^{-1}),
with $Q_0 = 1.635 \times 10^{-6}$ m^2 s^{-1}, having an asymptotic far-field thickness $H_0 = 100$
μm. These flow parameters give a value for N of 0.12 implying that the normal
component of gravity has little effect on the resultant free-surface shape. Also,
unless stated otherwise, the topography steepness factor, $\gamma = 0.01$, with automatic
mesh adaptivity starting at $k = 1$, utilising 4 levels of local refinement, the finest
grid level corresponding to $k = 5$ has $\Delta_5 = 1/1024$; $\varepsilon = 0.1\kappa_k$, where κ_k is the
L^2-norm of the residual on grid level k.

The first problem considered forms a useful benchmark and involves flow over
a rigid substrate containing a localised small square occlusion, with dimensions
$l_t = w_t = 1.54$, centered at $(x_t, y_t) = (30.77, 50)$; $L_c = L_0 = 0.78$ mm (for $\beta = 1$).
Both space adaptive and fixed fine mesh results were generated and comparisons
drawn with ones obtained for the same problem using the multigrid solver described
in [Lee, Thompson and Gaskell (2007)].

Fig. 2(a) shows a three-dimensional colour map and iso-contours of the result-
ing steady-state free-surface shape, clearly delineating the characteristic horse-shoe
bow-wave formed upstream of and surrounding the occlusion; just ahead of the oc-
clusion there is a gradual rise in the film height, up to a maximum value 16.5%
above the asymptotic film thickness at the point at which the film meets the oc-
clusion's upstream face. The height of the free-surface decreases away from this
maximum along its sides, dropping to a minimum value 6.1% below the asymp-
totic film thickness immediately behind and downstream of it. The streamwise
free-surface profile along $y = 50$, see Fig. 2(b), provides a quantitative measure of
the free-surface disturbance as well as highlighting the deviation, as a function of
the number of adaptive mesh levels employed, from the grid-independent reference
full mesh solution obtained using 1025×1025 points; in the vicinity of the up-
stream static wetting line the deviation is found to be 7.3%, 3.0% and 1.3% for
adaptive multigrid solutions with the finest grid level in each case corresponding
to $k = 2, 3$ and 4, respectively. With $k = 5$ both solutions correspond exactly. In
addition, it is interesting to note that the free-surface disturbance generated by this
small square occlusion is maintained significantly further downstream than is the

(a)

(b)
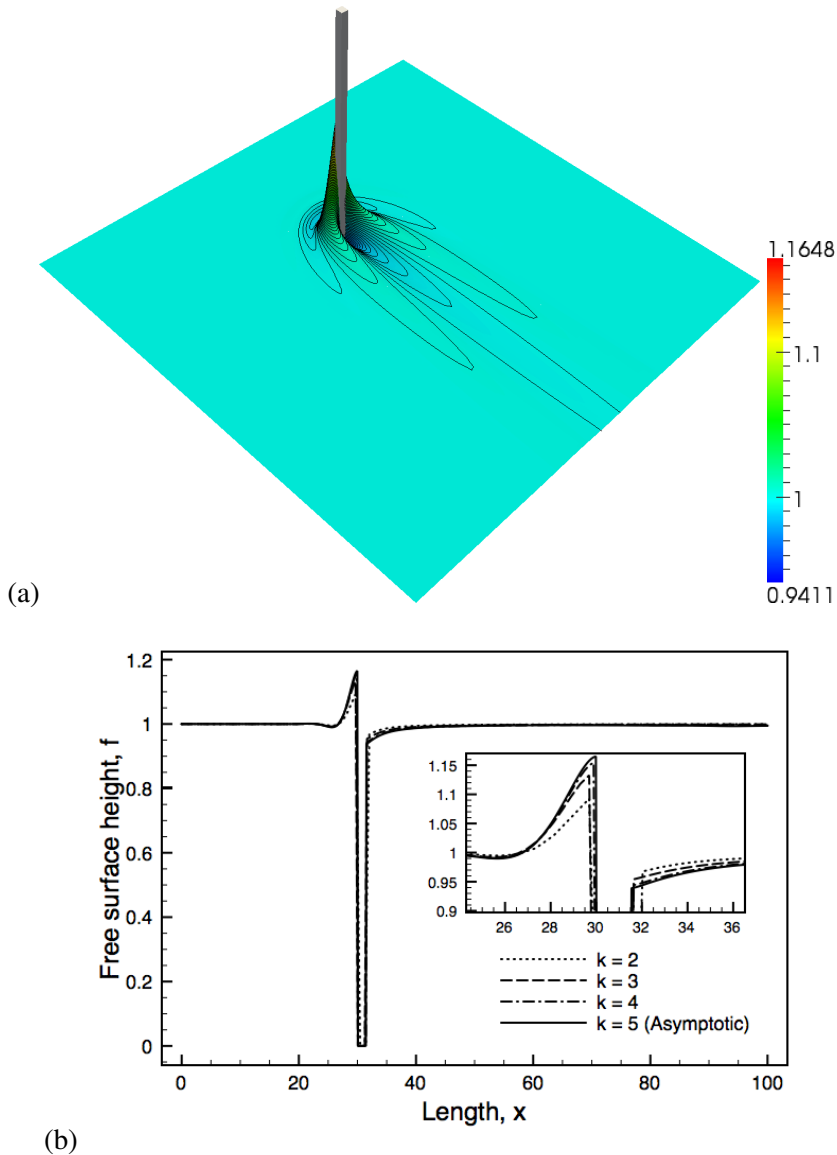
Figure 2: Flow past a small square occlusion: (a) three-dimensional colour map and iso-contours showing the steady-state free-surface disturbance which results; (b) steamwise free-surface profiles through the centre of the occlusion comparing the results obtained with different levels of local mesh refinement against the mesh independent solution obtained without the latter - the finest mesh in both cases corresponding to one having 1025×1025 points and $k = 5$. The flow direction in the top figure is from upper left to lower right, while in the bottom one it is from left to right.

case for a fully submerged square peak/trench topography of the same in-plane dimensions [Decré and Baret (2003); Gaskell, Jimack, Sellier, Thompson and Wilson (2004)].

Fig. 3 illustrates, in the form of iso-contours, the evolution of the free-surface, f, in time as it proceeds to steady-state. In order to aid visualisation of the corresponding adaptive mesh structures only two levels of mesh refinement are shown; the location of the occlusion is as indicated. Note that the same rule is applied to all subsequent figures showing adaptive meshes. A key feature of automatic adaptive local mesh refinement/de-refinement is that the mesh evolves with the solution, actively refining and de-refining in an error controlled manner at every time-step, following the development of the flow. The mesh structure at two different times and once steady-state is reached is shown in Figs. 3(b), (d) and (f), respectively. Figs. 3(a) and (b) reveal how the bow-wave initially forms upstream and bends to the left and right of the occlusion, while liquid surges past it displacing the same in the region immediately downstream of the obstruction forming a moving capillary ridge in the direction of flow that eventually exits the solution domain.

Fig. 4 shows that the multigrid strategy adopted achieves the desired O(N) efficiency (where N is the number of unknowns) and that in addition automatic mesh refinement leads to significant further computational savings. Although the proposed solver incurs a small overall penalty computation time wise, but less so when mesh adaptivity is employed, this is viewed as a small price to pay for increased flexibility and the general extendability of the approach. This is exemplified further in relation to the problems solved subsequently.

The next problem examines a case of transient flow for the same thin film of water past multiple occlusions comprised of a central blockage with a skewed elliptical cross section (rotated at 45° to the horizontal, with major and minor axes of dimensionless length 5.0 and 2.5, respectively, and centered at $(x_t, y_t) = (25, 50)$) and two rectangular blockages located slightly further downstream and to either side ($l_t = 10, w_t = 5$ centred at $(x_t, y_t) = (50, 2.5)$ and $(x_t, y_t) = (50, 97.5)$) forming part of the streamwise periodic boundary defined along $y = 0$ and $y = w_s$. The solution domain has dimensions $l_s = 200$ and $w_s = 100$.

Starting from the computed steady-state for flow past the system of occlusions, with $L_c = L_0 = 0.78$ mm ($\beta = 1$), the film thickness at the inlet boundary, $x = 0$, is then pulsed sinusoidally according to the expression:

$$h = 1 + \sin\left(\frac{2\pi t}{L_t}\right) \quad \text{for} \quad \left(0 \leq t \leq \frac{L_t}{2}\right), \tag{41}$$

with $L_t = 20$ specifying the periodic frequency, which generates the travelling wave shown in Fig. 5.
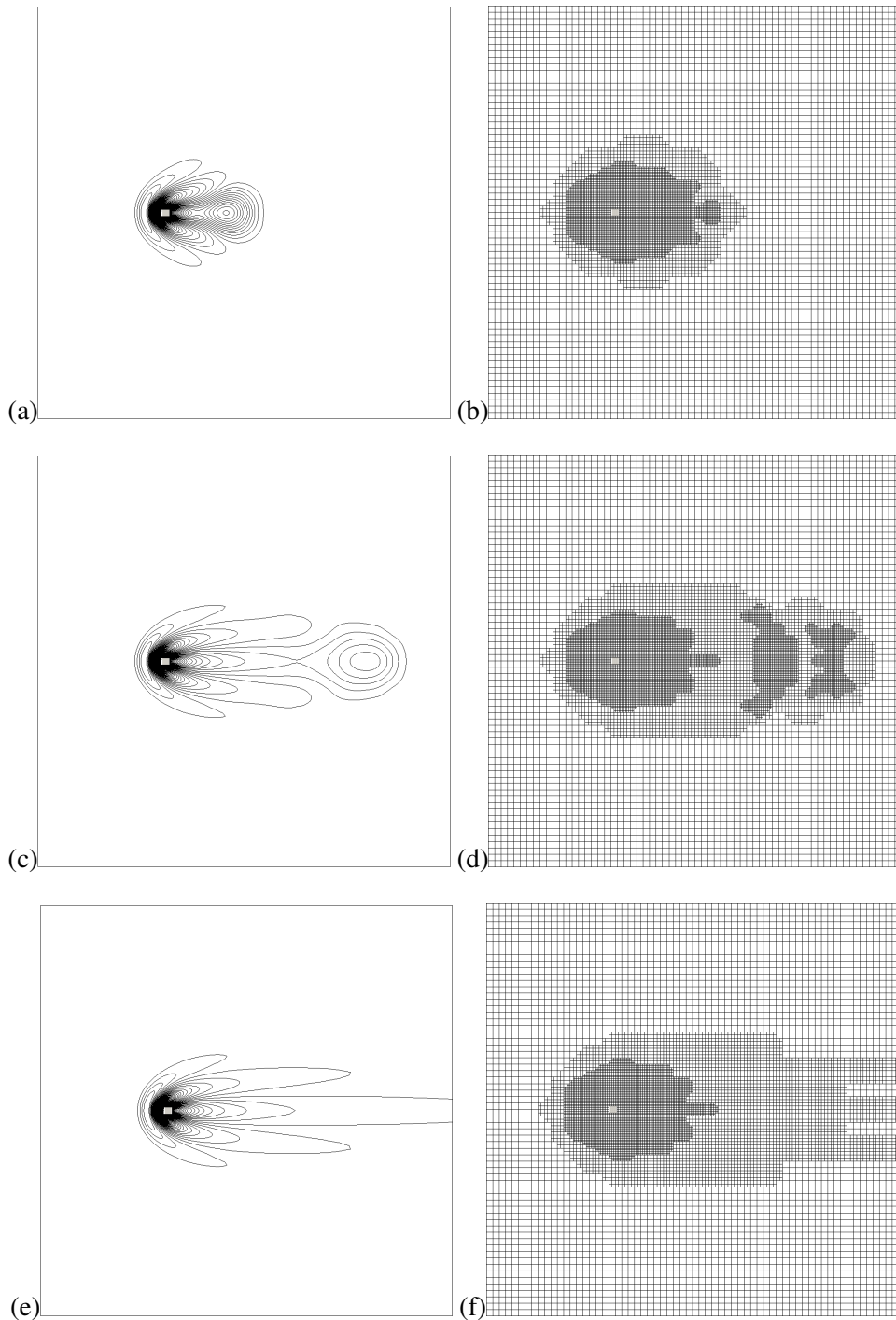
Figure 3: Evolution of the flow, from left to right, past a square occlusion shown at $t = 12$ (top), $t = 36$ (middle) and $t = 60$ corresponding to steady-state (bottom). Iso-contours (left); associated local mesh structures (right).
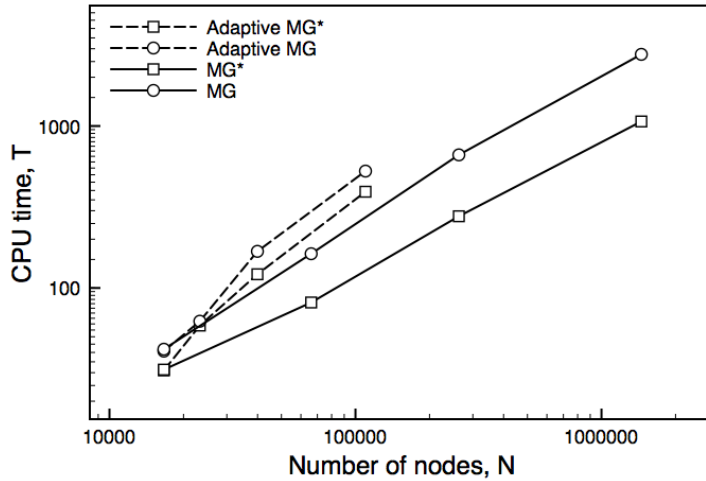
Figure 4: Flow past a small square occlusion. CPU time dependence on mesh density, comparing the results obtained with and without automatic local mesh refinement; the "*" denotes the corresponding solutions obtained with the multigrid method described in [Lee, Thompson, Gaskell (2007)].
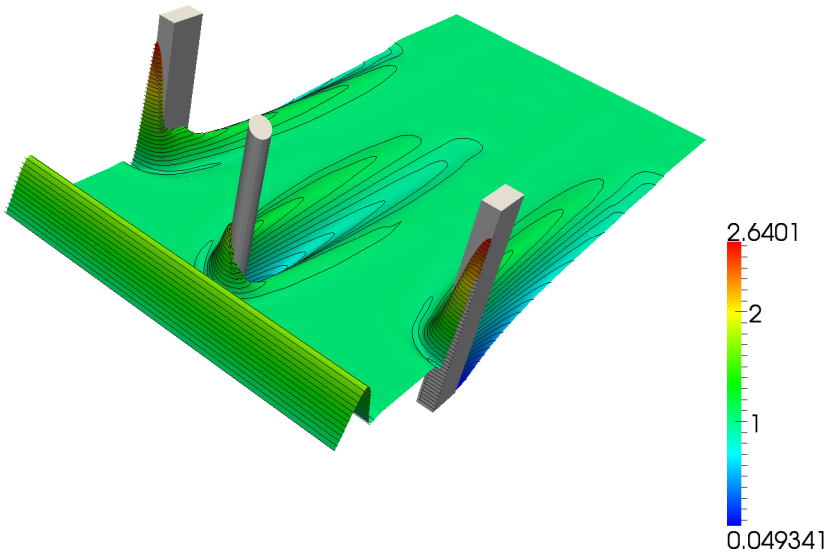
Figure 5: Free-surface colour map and iso-contours at the outset of pulsed flow through a system of occlusions comprised of a central skewed elliptical obstruction and two rectangular blockages starting from a condition of steady-state flow past the same. The direction of flow is from lower left to upper right.
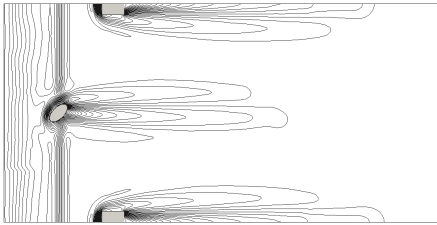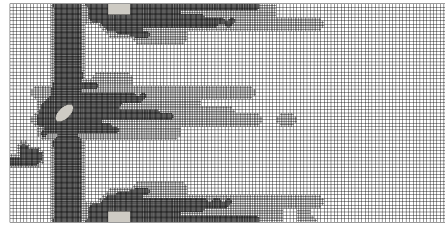
(a)   (b)
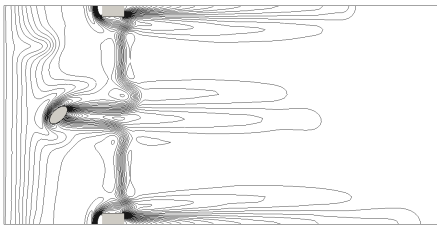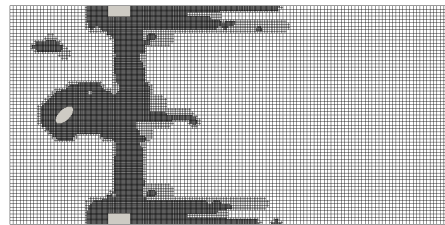
(c)   (d)
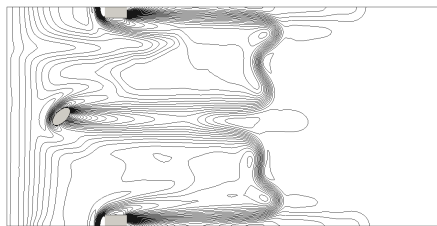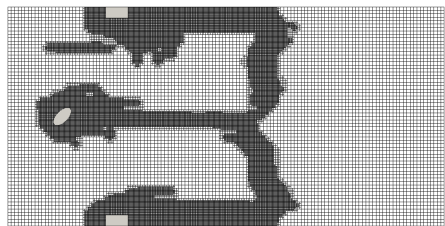
(e)   (f)

Figure 6: Evolution of pulsed flow through the system of occlusions shown in Figure 5. Free-surface iso-contours (left) and associated mesh structures (right) showing how the mesh automatically refines/de-refines as the solution progresses: $t = 5.22$ (top); $t = 14.36$ (middle); $t = 32.92$ (bottom). The direction of flow is from left to right.
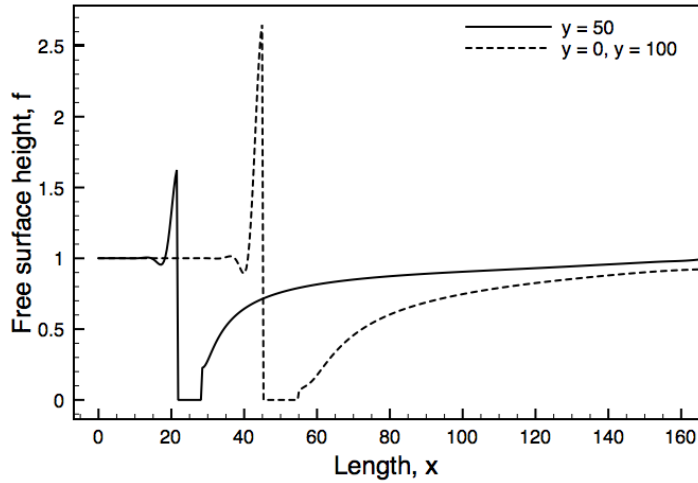
Figure 7: Final steady-state streamwise free-surface profiles through the centre of the skewed ellipse ($y = 50$, full line) and rectangular ($y = 0/100$, broken line) occlusion for flow through the system of occlusions shown in Figure 5. The direction of flow is from left to right.

Fig. 6 shows the free-surface response at various times in the form of contour maps, together with the corresponding local mesh structures, revealing very effectively the efficiency of the adaptive meshing procedure in coping with large and variable changes in the solution as the pulse travels through the occlusions. Note how the higher frequency fluctuation of the travelling wave tends to smooth out quite quickly due to surface tension effects in regions of high surface curvature. The latter effect is enhanced by the occlusions in that the free-surface of the pulsed disturbance is distorted further by the presence of the bow-waves upstream of them and which wrap around their sides; in particular, the disturbance caused by the skewed ellipse produces a free-surface asymmetry. The streamwise free-surface profiles along $y = 50.0$ and $y = 0.0/100.0$, shown in Fig. 7, reveal that there is respectively an approximate 78% and 95% reduction in film thickness just behind the two types of occlusion, while on their upstream side the disturbance is found to be respectively 60% and 165% greater than the far field asymptotic film thickness. It is important to be aware of the propensity for such effects which, in extreme cases, could lead to de-wetting behind an occlusion [Baxter, Power, Cliffe and Hibberd (2009)].

The flow of a thin water film past a splitter occlusion is considered next, the upstream edge of which is formed by a semi-circle of radius 0.05 centered at
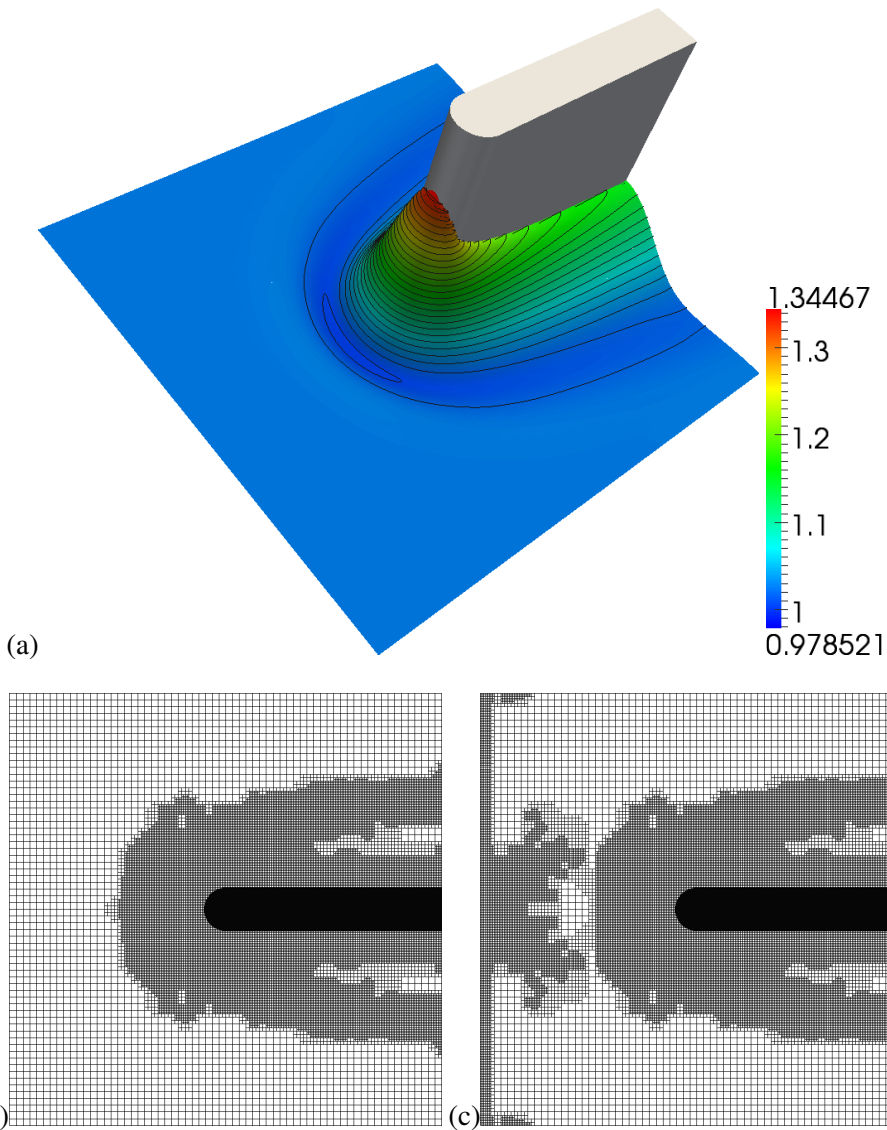
Figure 8: Flow past a splitter occlusion shown once steady-state is reached: (a) colour map and iso-contours of the free-surface disturbance; (b) the mesh structure associated with the former; (c) the corresponding mesh structure for the same flow conditions but when solute transport is included defined by $c = 0$ and 1 between $0 \le y \le 0.5$ and $0.5 \le y \le 1.0$, respectively at the inlet, $x = 0$. The flow direction in the top figure is from lower left to upper right, while in the lower one it is from left to right.
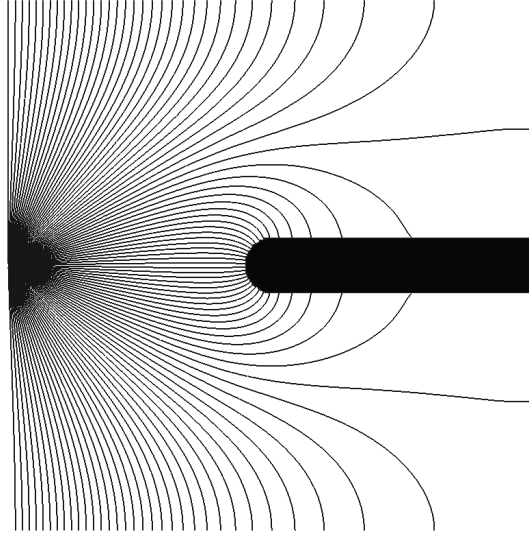
Figure 9: Iso-contours of solute concentration (defined by $c = 0$ and 1 between $0 \leq y \leq 0.5$ and $0.5 \leq y \leq 1.0$, respectively at the inlet, $x = 0$) for the case of flow past a splitter occlusion at steady-state, showing the symmetry of the same about the streamwise centre line. The flow direction is from left to right.

$(x_t, y_t) = (0.5, 0.5)$ with the the main body of it consisting of the rectangular region $0.5 \leq x \leq 1.0$ and $0.45 \leq y \leq 0.55$. The size of the solution domain is $l_s = 1, w_s = 1$, yielding a capillary length of, $L_c = 0.78$ mm; L_0 and β are set to 30.53 mm and 39.14, respectively. The resulting steady-state free-surface colour map and elevation contours are as shown in Fig. 8(a), revealing that the disturbance is comprised of a bow-wave upstream of the blunt-nosed splitter and a greatly elevated free-surface in the vicinity of the static wetting line. The maximum free-surface disturbance occurs at the upstream stagnation point on the splitter where the film thickness is found to be 34.5% greater than the asymptotic far field value; at the exit of the solution domain ($x = 1.0$) the difference between the maximum free-surface elevation and the far field film thickness has reduced markedly to 13.6%.

The addition of solute transport effects, via equation (14), leads to some interesting features with regard to mixing. The flow geometry remains the same with the solute concentration at the inlet ($x = 0$) given a value $c = 0$ between $0 \leq y \leq 0.5$ and $c = 1$ between $0.5 \leq y \leq 1.0$. The initial concentration everywhere else, prior to integrating forward in time, is taken to be $c = 0.5$. A contour plot of the resultant solute concentration at steady-state throughout the solution domain is shown in Fig. 9, which reveals that mixing occurs upstream of the film splitter occlusion

as expected. Fig. 10(a) shows the spanwise cross-sectional profile of the solute concentration at the exit, where $x = 1$, indicating the amount of mixing that occurs as a function of mixing length, x_m, defined as the distance between the inlet and the start of the occlusion. Notably, a uniform concentration level on either side of the splitter is only observed for the case when $x_m = 0.5$, suggesting that a minimum splitter length, l_t, with a value between 0.4 to 0.5 is required for this to be achieved. Extending the length of the domain to twice the original, taking cross-sectional profiles at $x = 2$, see Fig. 10(b), is seen to improve the uniformity of solute concentration at the outlets and shows that varying x_m can be used to control the resultant solute concentration level there while maintaining the uniformity of the same.

Since equation (14) is not coupled to the fluid flow equations, the f and p fields are unaffected and the resultant steady-state free-surface shape is the same; it does, however have a minor effect on the associated adaptive mesh structure, as shown in Figs. 8(b) and (c). Comparing the two, it can be seen that the bulk of the mesh refinement, which tracks the free-surface surrounding the occlusion, remains largely unchanged regardless of whether concentration gradients are involved; in the latter case, additional small amounts of refinement can be observed close to the inlet and centrally upstream of the occlusion, where fine scale resolution is necessary to capture the sharp changes in concentration gradient that occur there.

The complexity of the above flow problem is now further increased by replacing a section of the rigid substrate upstream of the splitter with a flexible patch, the size of which is taken to be $l_t = 0.375, w_t = 0.375$ centered at $x_t = 0.3125, y_t = 0.3125$; with $\lambda = 0.1$, $\rho_m = 1000$ kg m^{-3} and setting $\Upsilon = 1$. Its introduction, modelled via equation (15), which unlike the concentration equation is coupled with the flow equations, has a significant and direct impact on the resulting steady-state free-surface disturbance. As shown in Fig. 11(a), the dynamic solid-liquid interaction involved results in flow asymmetry. In particular, the additional liquid lying above the flexible patch leads to a skewing of the maximum free-surface elevation to the side of the splitter having the patch located upstream of it and is 51.7% greater than the asymptotic far-field value. The maximum free-surface elevation on either side of the splitter at the exit ($x = 1.0$) is 15.6% and 11.4%, the former corresponding to the side containing the upstream flexible patch. The inclusion of the latter also produces a slight dip in film height across it, leading to a minimum free-surface disturbance there 3.6% below the asymptotic far field value. Fig. 11(b) shows a colour map and iso-contours of the deformation experienced by the flexible patch, whose shape is influenced by the height of the liquid film above it; the maximum and minimum deflection of the patch away from an equivalent rigid planar substrate being 4.7% and 8.7%, respectively.

The flexible patch also has an impact on the mixing that takes place, albeit small,

as indicated by the contour levels in Fig. 12, contributing to a change in solute concentration levels at the exit; the results is a 1% difference to the overall solute mix achieved when $x_m = 0.5$ compared to the case where no flexible patch is present. Fig. 11(c) shows the corresponding adaptive mesh structure at steady-state.

Earlier, the general overall numerical procedure was shown to possess the desired O(N) efficiency for the benchmark case of flow around a single square occlusion. The same is now examined in relation to the the film-splitter problem by successively adding additional physical effects, mirroring each of the scenarios examined above. The results, presented in Fig. 13, show the same O(N) efficiency to be maintained. There is, as expected, a corresponding increase in the amount of CPU expended as the number of equations to be solved increases. Taking the lubrication equations, (5) and (6), as the base line, including the solution of the concentration equation (14), and then in addition equation (15) for substrate deflection, leads to corresponding increases of 25% and 41%, respectively in the CPU time required to produce accurate solutions.

Considered next is an example of thin film flow over a complex inter-connected topographical feature, formed from the addition and subtraction of simple topography primitives and occlusions as discussed in Section 2. The flow investigated is associated with the photolithographic fabrication of a micro-patterned micro-fluidic device [Tourovskaia, Figueroa-Mason and Folch (2006)], the goal being to maximise the planarity of the photoresist film. The liquid in this particular case has the following properties: viscosity $\mu = 8.928$ Pa s, density $\rho = 1123$ kg m^{-3} and surface tension $\sigma = 0.048$ N m^{-1}. The asymptotic film thickness is $H_0 = 100$ μm, corresponding to a uniform flow rate per unit width of $Q_0 = 2.0566 \times 10^{-10}$ m^2 s^{-1}; the values taken for L_c and β are 6.6227×10^{-4} m and 15.1, respectively, giving $N = 0.144$. The complex topography involved, shown in Fig. 14(a), covers an area of 10 mm $\times$ 15 mm in size and is 25 μm heigh other than where the occlusions that form part of it are located; the flow is solved on a square $l_s = w_s = 3$ (30 mm $\times$ 30 mm) computational domain.

Fig. 14(b) shows the steady-state free-surface disturbance that result. Notably, it is not the submerged surface topography that dictates the nature of the disturbance; the dominant flow features arise from the characteristic bow-waves formations that results from flow past the circular occlusions. The combined effect of the bow-wave and the depressions in their wake is clear from the colour map and iso-contours of Fig. 15(e), where the sum of the individual disturbances give rise to the largest free-surface elevation occurring at the bottommost occlusion (82.2%) and the largest depression (-38.4%) just downstream of the leading occlusion at the left hand side of the domain, indicated by "$\times$" and "O", respectively. Illustrated also is the effect of orientating the topography, relative to the direction of flow, on the resulting
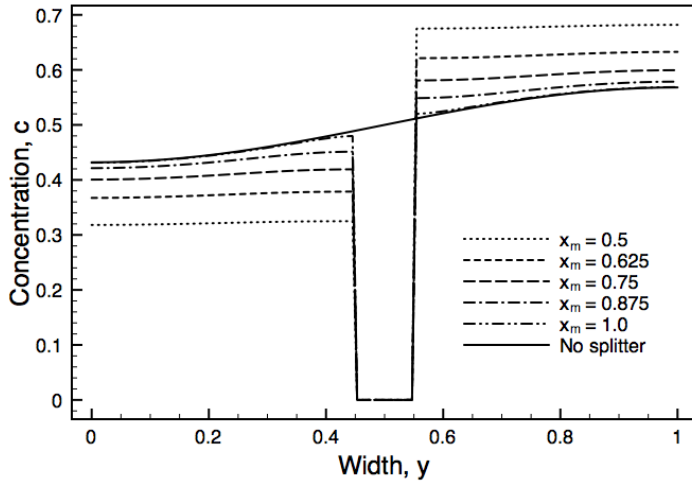
(a)
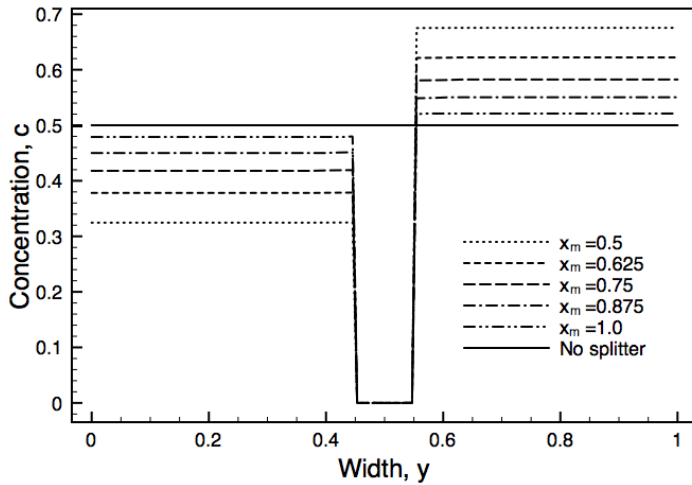
(b)

Figure 10: Flow, with solute transport (defined by $c = 0$ and 1 between $0 \le y \le 0.5$ and $0.5 \le y \le 1.0$, respectively at the inlet $x = 0$) past a splitter occlusion. Spanwise plots, at steady-state, at the exit of the domain as a function of the mixing length x_m: (a) on a square solution domain, $x = 1.0$; (b) when the solution domain is doubled in length, $x = 2.0$.
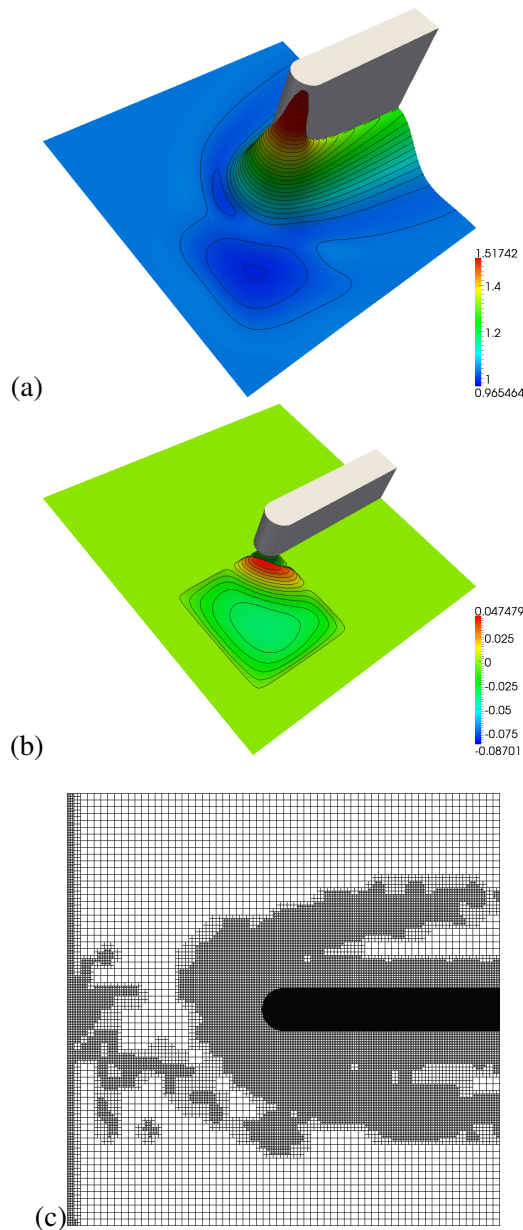
Figure 11: Flow past a splitter occlusion including solute transport (defined by $c = 0$ and 1 between $0 \leq y \leq 0.5$ and $0.5 \leq y \leq 1.0$, respectively at the inlet $x = 0$) together with a flexible patch on the substrate located as shown, once steady-state is reached: Colour map and iso-contours of (a) the free-surface disturbance and (b) the deformation experienced by the flexible patch; (c) the corresponding mesh structure. The flow direction in the top two figures is from lower left to upper right, while in the bottom one it is from left to right.
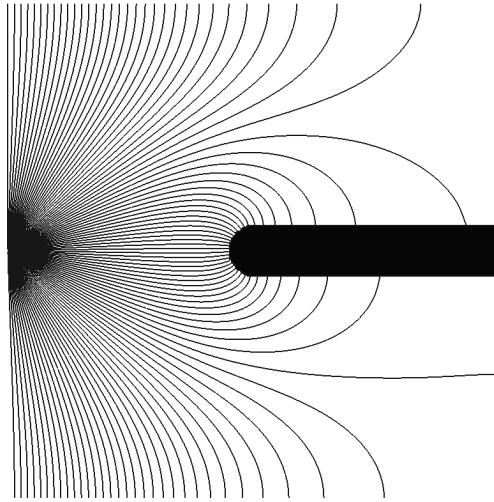
Figure 12: Iso-contours of solute concentration (defined by $c = 0$ and 1 between $0 \leq y \leq 0.5$ and $0.5 \leq y \leq 1.0$, respectively at the inlet, $x = 0$) for the case of flow past a splitter occlusion at steady-state when a flexible patch is present upstream of it. Note the asymmetry induced by the former, c.f. Figure 9. The direction of flow is from left to right.
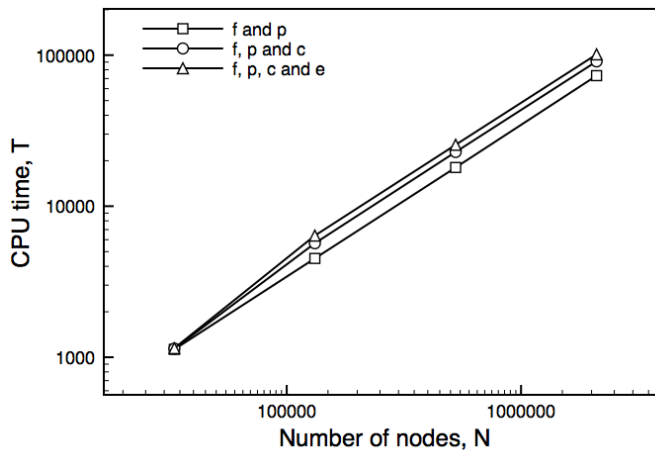
Figure 13: Flow past a splitter occlusion as the physical effects incorporated are increased. CPU time dependence on mesh density, comparing the efficiencies obtained when (i) just the base flow lubrication equations for f and p, (ii) as for (i) together with the solute concentration equation for, c, and finally (iii) as for (i) and (ii) plus the effect of substrate deformation equation for, e, are solved for.

(a)

(b)
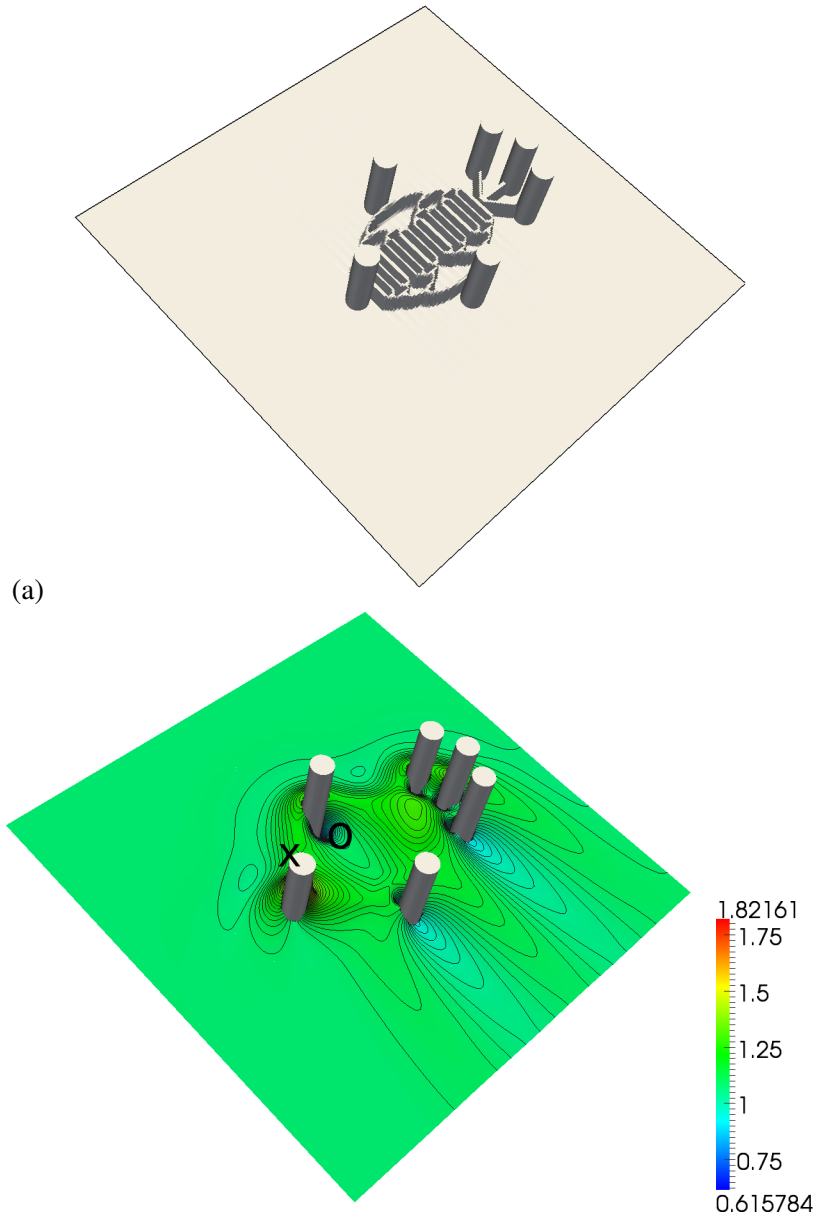
Figure 14: Flow over a complex micro-fluidic interconnected topographical feature constructed using a series of simple primitive shapes and occlusions defined on a square computational domain: (a) schematic of the geometry involved; (b) Colour map and iso-contours of the resulting free-surface disturbance at steady-state - the "×" and "O" denote the location of the maxima and minima disturbance away from the asymptotic far-field film thickness. The direction of flow is from upper left to lower right.
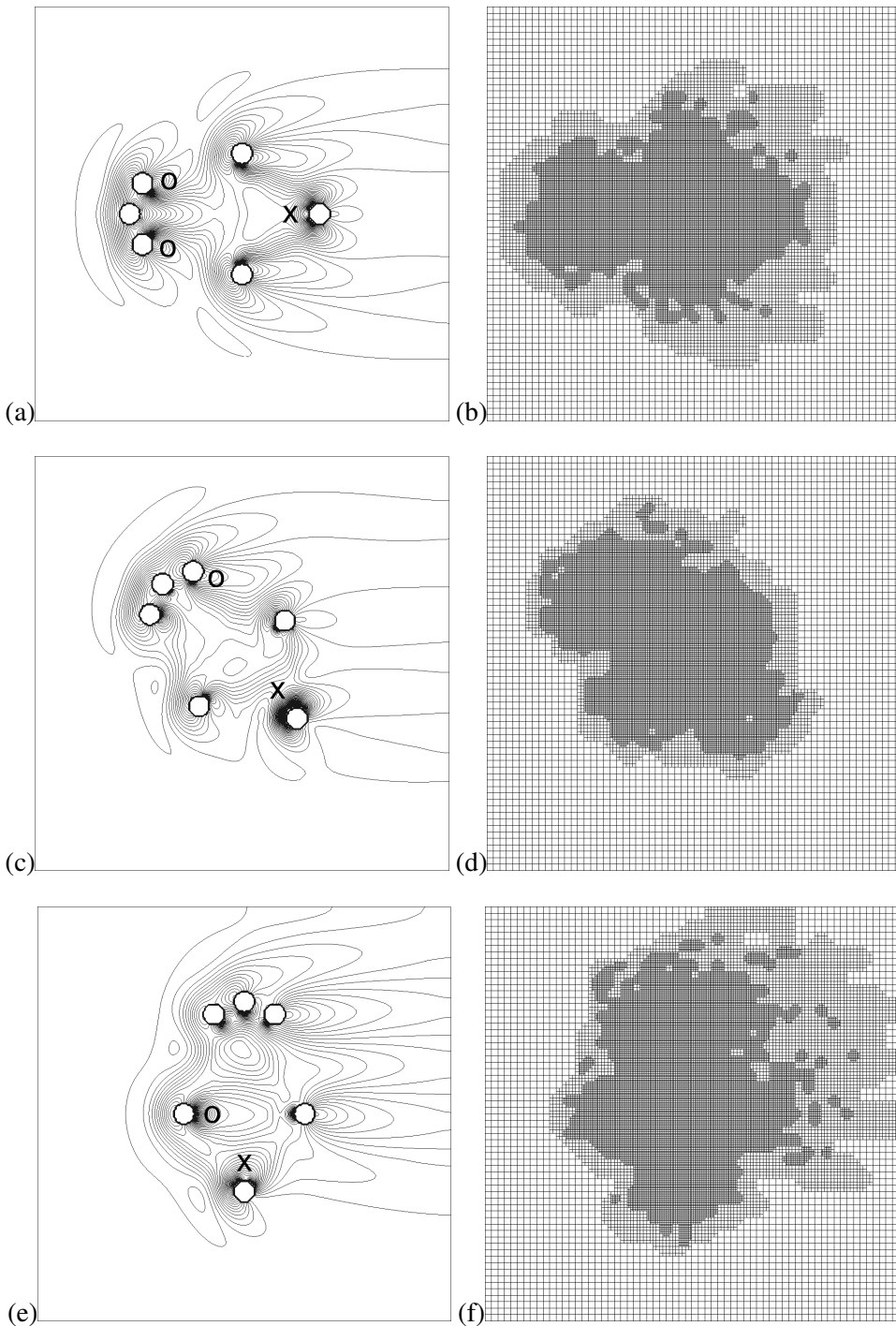
Figure 15: Flow over the complex interconnected topographical feature, Figure 14(a), showing the location of largest ($\times$) and smallest (O) free-surface disturbance away from that of the asymptotic far field film thickness (left) and the corresponding underlying mesh structure (right), as a function of the inlet orientation angle: -90° (top); -45° (middle); 0° (bottom). Flow direction is from left to right.
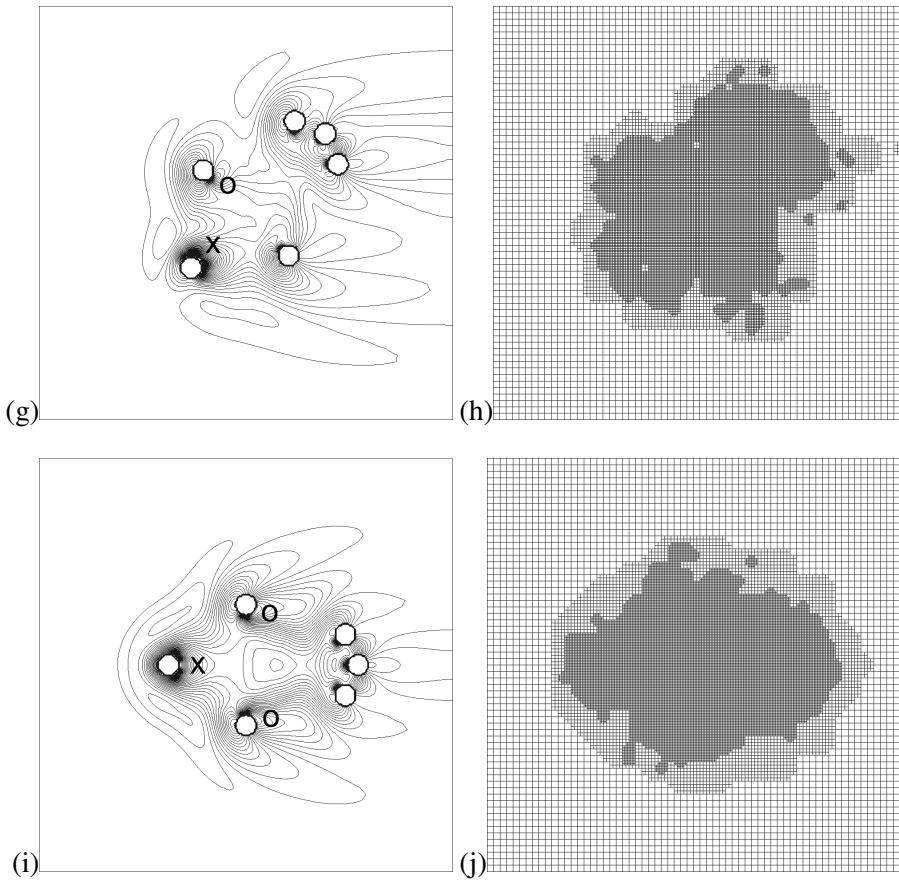
Figure 15: continued. Flow over the complex interconnected topographical feature, Figure 14(a), showing the location of largest ($\times$) and smallest (O) free-surface disturbance away from that of the asymptotic far field film thickness (left) and the corresponding underlying mesh structure (right), as a function of the inlet orientation angle: 45° (top); 90° (middle); 0° (bottom). Flow direction is from left to right.

(a)   (b)

(c)   (d)
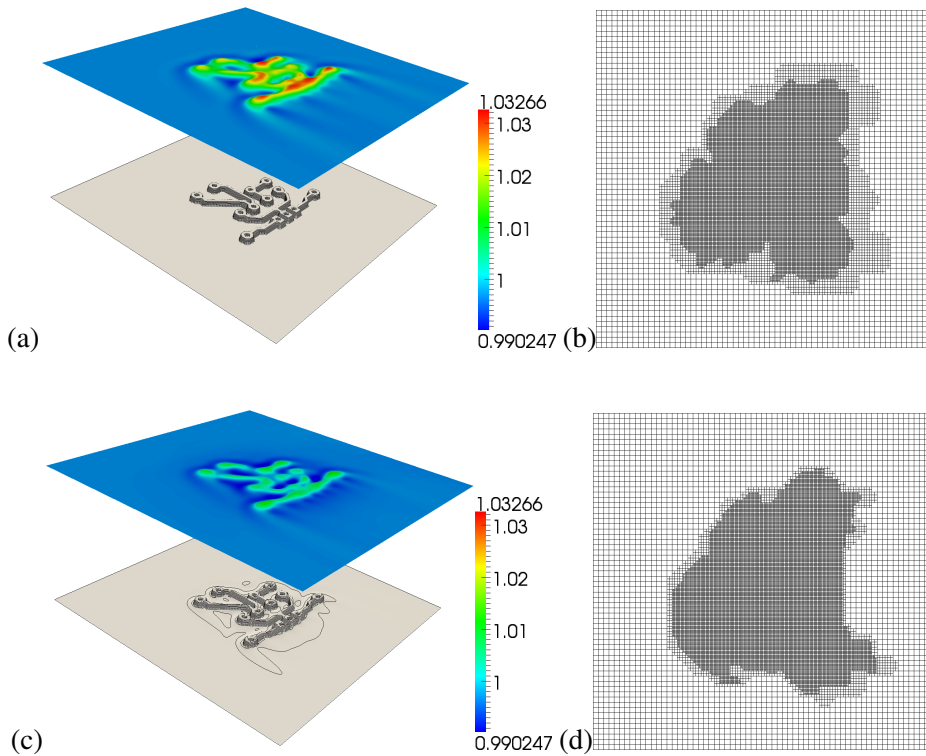
Figure 16: Flow over an interconnected micro-ciruit like topography positioned on both rigid and flexible substrate: colour maps and iso-contours of the resulting free surface disturbance together with the topography definition and deformation experienced in the case of a flexible substrate at steady-state (left); associated adaptive mesh structure (right).

free-surface disturbance, showing the position of the associated free-surface maxima and minima – see Fig. 15. Included in this figure for completeness are the corresponding steady-state adaptive mesh configurations in each case. Note that, as discussed in [Sellier, Lee, Thompson and Gaskell (2009)], the wake structure that is generated persists far downstream and a solution domain approximately 3 to 4 times larger than the section shown was necessary to ensure that it did not extend beyond the outflow boundary.

The final problem investigated explores the case of the flow of a thin water film over both a rigid and flexible substrate containing a complex interconnected topography reminiscent of a micro-circuit. The topography covers an area given by $(l_t \times w_t) =$

(0.5×0.8), is $5\,\mu$m in height and placed at the centre of a $l_s = w_s = 2$ square solution domain with $L_c = 0.78$ mm and $\beta = 39.14$.

Fig. 16(a) shows the resulting steady-state free-surface colour map of the disturbance generated when the surface containing the circuit, shown below it, is rigid, $\Upsilon = \infty$. The corresponding free-surface disturbance when the substrate containing the circuit is flexible, $\Upsilon = 1$ and $\lambda = 0.5$, is shown in Fig. 16(c). It can be seen clearly that substrate flexibility leads to a significant reduction in the overall free-surface disturbance generated, having a positive effect in relation to free-surface planarisation. Notably, it is the small localised deflections of the flexible substrate, having maximum value of 0.5% and minimum value of 3.3% from the point of zero deflection, which lead to this reduction – by as much as 53.5%, compared to the situation when the substrate is rigid. The deformation experienced by the flexible substrate itself, is indicated by the iso-contours in Figs. 16 (c). The associated resulting automatic adaptive mesh structures are shown in Figs. 16(b) and (d). Although they look quite similar, the flexible substrate solution requires the use of a finer mesh over a greater area. As in the previous example it would be a relatively simple to task to explore changes to the free-surface deformation resulting as a consequence of altering the orientation of the circuit relative to the flow direction, and to thus identify the flow configuration required to achieve optimum planarisation of the free-surface.

5   Conclusion

A coupled system of equations resulting from the application of the long-wave approximation to the governing Navier-Stokes equations is solved for the case of gravity driven three-dimensional thin film flow on substrates containing topography. The latter can be either completely engulfed by the liquid layer and/or extend all the way through it. The numerical procedure described and utilised to solve their discrete analogue makes use of the desirable attributes of adopting an efficient, tried and tested multigrid framework, including both automatic error controlled adaptive time-stepping and local mesh refinement/de-refinement, combined with a generally applicable Newton globally convergent iterative routine. The latter forms a key component of the overall solution strategy, since it readily facilitates and greatly simplifies the embodiment and solution of additional single, or multiple, coupled or otherwise, equations representing further physics and having the same form as the base flow lubrication equations.

The above approach is used to solve a hierarchy of problems and found to be very flexible and robust. They range in complexity from the case of thin film flow on rigid substrates containing simple and complex topography and/or single or multiple occlusions, to ones involving additional physics in the form of solute transport

together with cases when the substrate itself, or parts of it, is taken to be flexible. The proposed general purpose numerical procedure:

- Is shown to perform well in all cases, with the benefits of automatic mesh adaption in particular being abundantly clear. The numerical efficiency achieved across the board is found to be O(N), where N is the number of unknowns, as expected from a well posed multigrid based algorithm.

- Provides a convenient methodology for the modelling and investigation of a wider range of complex, three-dimensional thin film flow problems than has been considered hitherto. For example, it could be exploited in medical applications concerned with optimising the delivery of drug laden films or more generally in the broader area of droplet motion/coalescence which has enormous significance with respect to the spreading of inks and the deposition of bio-pesticides. Last but not least, the control of thin film flows in the context of predicting the conditions for achieving maximum free-surface planarisation is important in relation to the direct patterning of functional layers apropos micro-chip production.

6 References

Baxter, S.J.; Power, H.; Cliffe, K.A.; Hibberd, S. (2009): Three-dimensional thin film flow over and around an obstacle on an inclined plane. *Phys. Fluids*, vol. 21, no. 3, pp. 032102-032102-23.

Blyth, M.G.; Pozrikidis, C. (2006): Film flow down an inclined plane over a three-dimensional obstacle. *Phys. Fluids*, vol. 18, pp. 052104.

Craster, R.V.; Matar, O.K. (2009): Dynamics and stability of thin liquid films. *Rev. Mod. Phys.*, vol. 81, no. 3, pp. 1131-1197.

COMSOL® (2008) Multiphysics 3.5.

Daniels N.; Ehret P.; Gaskell P.H.; Thompson H.M.; Decré M.M.J. (2001): Multigrid methods for thin film spreading flows. *Proc 1st Conf on Computational Fluid Dynamics (editor N. Satofuka)*, pp. 279-284.

Decré, M.M.J.; Baret, J.C. (2003): Gravity-driven flows of viscous liquids over two-dimensional topographies. *J. Fluid Mech.*, vol. 487, pp. 147-166.

Diez, J.A.; Kondic, L. (2002): Computing three-dimensional thin film flows including contact lines. *J. Comput. Phys.*, vol. 183, pp. 274-306.

Gaskell, P.H.; Jimack, P.K.; Sellier, M.; Thompson, H.M. (2004): Efficient and accurate time adaptive multigrid simulation of droplet spreading. *Int. J. Num. Meth. Fluids.*, vol. 45, pp. 1161-1186.

Gaskell, P.H.; Jimack, P.K.; Sellier, M.; Thompson H.M. (2006): Flow of evaporating gravity-driven thin liquid films over topography. *Phys. Fluids*, vol. 18, pp. 013601.

Gaskell, P.H.; Jimack, P.K.; Sellier, M.; Thompson, H.M.; Wilson, M.C.T. (2004): Gravity-driven flow of continuous thin liquid films on non-porous subsrates with topography. *J. Fluid Mech.*, vol. 509, pp. 253-280.

Hayes, M.; O'Brien, S.B.G.; Lammers, J.H. (2000): Green's function for steady flow over a small two-dimensional topography. *Phys. Fluids*, vol. 12, no. 11, pp. 2845-2858.

Howison, S.D.; Moriarty, J.A.; Ockendon, J.R.; Terril, E.L.; Wilson, S.K. (1997): A mathematical model for drying paint layer. *J. Eng. Math.*, vol. 32, pp. 377.

Lee, Y.C.; Thompson, H.M.; Gaskell, P.H. (2007): An efficient adaptive multigrid algorithm for predicting thin film flow on surfaces containing localised topographic features. *Comp. Fluids*, vol. 36, no. 838-855.

Lee, Y.C.; Thompson, H.M.; Gaskell, P.H. (2008): The efficient and accurate solution of continuous thin film flow over surface patterning and past occlusions. *Int. J. Num. Meth. Fluids*, vol. 56, no. 8, pp. 1375-1381.

Lee, Y.C.; Thompson, H.M.; Gaskell, P.H. (2009): Thin film flow over flexible membranes containing surface texturing: bio-inspired solutions, *J. Eng. Tribo. IMechE Part J.*, vol. 223, no.3, pp. 337-345.

Peurrung, L.M.; Graves, D.B. (1991): Film thickness profiles over topography in spin coating. *J. Electrochem. Soc.*, vol. 138, pp. 2115-2124.

Pozrikidis, C.; Thoroddsen, S.T. (1991): The deformation of a liquid-film flowing down an inclined plane wall over a small particle arrested on the wall. *Phys. Fluids*, vol. 3, pp. 2546-2558.

Press, W.H.; Teukolsky, S.A.; Vetterling, W.T.; Flannery, B.P. (2003): *Numerical Recipes in C*. Cambridge University Press.

Sellier, M.; Lee, Y.C.; Thompson, H.M.; Gaskell, P.H. (2009): Thin film flow on surfaces containing localized arbitrary occlusions. *Comput. Fluids*, vol. 38, no. 1, pp. 171-182.

Stillwagon, L.E.; Larson, R.G.; Taylor, G.N. (1988): Fundamentals of topographic leveling. *J. Appl. Phys.*, vol. 64, no. 11, pp. 5251-5258.

Tourovskaia, A.; Figueroa-Mason, X.; Folch, A. (2006): Long-term Microfluidic Cultures of Myotube Microarrays for High-Throughput Focal Stimulation. *Nature Protocols*, vol. 1, no. 3, pp. 1092.

Trottenberg, U,; Oosterlee C.W.; Schüller A. (2001): *Multigrid*, Academic Press.

Veremieiev, S.; Thompson, H.M.; Lee, Y.C.; Gaskell, P.H. (2010a): Inertial thin film flow on planar surfaces featuring topography. *Comput. Fluids*, vol. 39, pp 431-450.

Veremieiev, S.; Thompson, H.M.; Lee, Y.C.; Gaskell, P.H. (2010b): Three-dimensional inertial film flow on planar substrates containing occlusions. *Proceedings of the 5th European Conference on Computational Fluid Dynamics* ECCO-MAS CFD 2010, J.C.F Pereira and A. Sequeira (eds.), Lisbon, Portugal, article no. 01399.